Momentum-space structure of dineutrons in Borromean nuclei

Masayuki Yamagami
Department of Computer Science and Engineering, University of Aizu, Aizu-Wakamatsu, Fukushima 965-8580, Japan

(Received 20 April 2022; revised 11 August 2022; accepted 26 September 2022; published 17 October 2022)

A comparative study is made of the momentum-space structure of dineutrons in the Borromean nuclei ^{11}Li, ^{6}He, ^{22}C, and ^{19}B. The ground-state properties of these nuclei are well described by a three-body model using a newly constructed finite-range *nn* interaction in momentum space. I clarify how the mean opening angle between momenta of valence neutrons and the opening-angle distribution reflect the two-neutron density of the Borromean nuclei. By indicating the similarities to the distributions for the correlation angle in the knockout-reaction experiments, I show that the angular correlations of halo neutrons can provide rich information for the characteristic structure of dineutrons in the Borromean nuclei.

DOI: 10.1103/PhysRevC.106.044316

I. INTRODUCTION

The geometry of the two-neutron ($2n$) Borromean nuclei has attracted attention in recent decades [1–4]. The long core-n distance is characterized by the low-density neutron halo and the narrow momentum distributions of the decay fragments in breakup experiments. The core plus $2n$ system is bound due to the effective *nn* correlations in low-density medium, and many studies have been made to clarify the nature of the *nn* correlation, i.e., whether or not it corresponds to dineutrons in which spatial correlations are maximum.

The drastic change of the correlation length of $2n$ pairs with the matter density was shown by Hartree-Fock-Bogoliubov calculations [5]. Consequently, the dineutron correlation was predicted in dilute neutron-rich matter below the saturation density ρ_0 of $10^{-4} \lesssim \rho/\rho_0 \lesssim 0.5$. Following this consideration, the authors of Ref. [6] showed that the dineutron correlation should appear at the surface of the $2n$ halo nuclei (see, e.g., Ref. [7] for a recent review, and references therein).

One pioneer study is the measurement of the low-lying electric dipole ($E1$) transition strength in ^{11}Li [8]. By relating to the $E1$ cluster sum rule, the distance between the core and the center of mass of valence neutrons (the core-$2n$ distance) and the opening angle between position vectors of valence neutrons were extracted. Similar analyses have been made for ^{6}He [9,10] and ^{19}B [11]. The core-$2n$ distance was also extracted by associating with the charge radius in ^{11}Li [12–14]. The distance between valence neutrons (the n-n distance) was measured for ^{6}He, ^{11}Li, and ^{14}Be based on the Hanbury Brown–Twiss correlation study [15,16].

Information about the structure of dineutrons in momentum space plays a complementary role by viewing it from different perspectives. A recent knockout-reaction experiment for ^{11}Li measured the mean correlation angle between momenta of the two emitted neutrons [17]. The mean correlation angle is considered to reflect the momentum-space structure of dineutrons.

Besides numerous investigations of the real-space structure of Borromean nuclei, few calculations have been performed in momentum space. The three-body Faddeev equations were solved in momentum space for ^{11}Li and ^{6}He [18–21]. The momentum distributions of the decay fragments in breakup experiments were the main interest.

The calculation in momentum space itself has advantages for description of weakly bound nuclei. For example, the model space can be tiny, because the wave function with spatially extended structure in real space, via the uncertainty principle, translates into a narrow distribution in momentum space. The advantages were demonstrated in a quasiparticle random phase approximation calculation using the Skyrme energy density functional [22].

The construction of effective interactions is an important factor in advancing the study of unstable nuclei. The density-dependent contact $\delta(\mathbf{r})$ interaction is easy to handle, and widely used for pairing problems in the density functional theory (DFT) [23,24] and the three-body model [1,25,26]. The contact $\delta(\mathbf{r})$ pairing interaction can be meaningful with a cutoff energy in the two-particle spectrum $\varepsilon_1 + \varepsilon_2 \leqslant E_{\rm cut}$, although the principal prescription for determining the cutoff energy has not been established. A cutoff energy in the range from 15 to 120 MeV was often used (see, e.g., Refs. [26–29]), but the pair wave function does not converge, via the uncertainty principle, with increasing $E_{\rm cut}$ (see, e.g., Refs. [5,26]).

In the present study, an effective finite-range *nn* interaction in momentum space is constructed with the intention of wide application including DFT calculations. By performing the three-body model calculation for the Borromean nuclei ^{11}Li, ^{6}He, ^{22}C, and ^{19}B, I demonstrate the descriptive power of the new *nn* interaction. I clarify how the mean opening angle and the opening-angle distribution reflect the structure of dineutrons in the Borromean nuclei.

This paper is organized as follows. In Sec. II, the three-body model is explained. In Sec. III, the effective *nn* interaction is constructed. In Secs. IV and V, the ground-state properties and the dineutron structure in ^{11}Li and ^{6}He are discussed. In Secs. VI and VII, the three-body model is applied to ^{22}C and ^{19}B. Conclusions are drawn in Sec. VIII.

II. METHOD

A. Three-body model

I consider a three-body system consisting of an inert core nucleus with the mass number A_c and two valence neutrons n_1 and n_2. The three-body Hamiltonian in momentum space is defined by

$$H = h_{cn}(1) + h_{cn}(2) + V_{nn} + \frac{\hbar^2}{A_c m}\mathbf{k}_1 \cdot \mathbf{k}_2. \tag{1}$$

Here, h_{cn} is a core-n single-particle Hamiltonian, m is the neutron mass, and $\mathbf{k}_1$, $\mathbf{k}_2$ are momenta of valence neutrons. ($\mathbf{k}$ is called momentum together with $\hbar\mathbf{k}$.) V_{nn} is an effective nn interaction. The last term in Eq. (1) represents the recoil kinetic energy of the core [26].

For h_{cn}, the Schrödinger equation for the radial single-particle wave function $\psi_{n_r l j}(k)$ of angular-momentum quantum numbers l, j is an integral equation [30],

$$\frac{\hbar^2 k^2}{2\mu}\psi_{n_r l j}(k) + \frac{2}{\pi}\int_0^\infty V_{lj}(k,p)\psi_{n_r l j}(p)p^2 dp = \varepsilon_{n_r l j}\psi_{n_r l j}(k). \tag{2}$$

Here, n_r is the radial quantum number, $\mu = mA_c/(A_c+1)$ is the reduced mass, and $\varepsilon_{n_r l j}$ is the single-particle energy. The core-n potential is given by

$$V_{lj}(k,p) = \int_0^\infty j_l(kr)V_{lj}(r)j_l(pr)r^2 dr, \tag{3}$$

with the Woods-Saxon potential

$$V_{lj}(r) = V_0\left[1 - 0.44 f_{ls} r_0^2 (\boldsymbol{l}\cdot\boldsymbol{s})\frac{1}{r}\frac{d}{dr}\right] \times \left[1 + \exp\left(\frac{r - R_{cn}}{a_{cn}}\right)\right]^{-1}. \tag{4}$$

j_l is the spherical Bessel function, and $R_{cn} = r_0 A_c^{1/3}$. The parameters V_0, r_0, a_{cn}, and f_{ls} will be given in Secs. IV, VI, and VII.

The ground-state wave function of the three-body Hamiltonian H is given by

$$\Psi_{gs}(\mathbf{k}_1,\mathbf{k}_2) = \sum_{n_1 n_2 l j} \alpha_{n_1 n_2 l j}\Psi^{(2)}_{n_1 n_2 l j}(\mathbf{k}_1,\mathbf{k}_2). \tag{5}$$

The expansion coefficient $\alpha_{n_1 n_2 l j}$ is found by diagonalizing H in the model space of the two-neutron states with the energy $\varepsilon_1 + \varepsilon_2 \leqslant E_{\text{cut}}$. The uncorrelated two-neutron wave function $\Psi^{(2)}_{n_1 n_2 l j}(\mathbf{k}_1,\mathbf{k}_2)$ coupling to total angular momentum $J = 0$ can be constructed in a manner similar to the real-space calculation [1,26].

The $2n$ density distribution in momentum space is defined by $\rho_2(\mathbf{k}_1,\mathbf{k}_2) = |\Psi_{gs}(\mathbf{k}_1,\mathbf{k}_2)|^2$. The $2n$ density distribution in real space is obtained by the Fourier transformation

$$\rho_2(\mathbf{r}_1,\mathbf{r}_2) = \frac{1}{(2\pi)^3}\int d^3k_1 d^3k_2 e^{i\mathbf{k}_1\cdot\mathbf{r}_1 + i\mathbf{k}_2\cdot\mathbf{r}_2}\rho_2(\mathbf{k}_1,\mathbf{k}_2). \tag{6}$$

The root-mean-square (RMS) values of the core-$2n$ distance $\bar{r}_{c\text{-}2n} = \sqrt{\langle|(\mathbf{r}_1+\mathbf{r}_2)^2/4\rangle|}$ and the n-n distance $\bar{r}_{nn} = \sqrt{\langle|(\mathbf{r}_1-\mathbf{r}_2)^2\rangle|}$ are calculated by using Eq. (6). The matter radius R_m of the three-body system with mass number $A = A_c + 2$ [1,26] is obtained by

$$(R_m)^2 = \frac{A_c}{A}(R_c)^2 + \frac{2A_c}{A^2}(\bar{r}_{c\text{-}2n})^2 + \frac{1}{2A}(\bar{r}_{nn})^2. \tag{7}$$

Here, R_c is the radius of the core nucleus.

III. EFFECTIVE *nn* INTERACTION

I construct an effective nn interaction in momentum space for pairing correlations. First, a nonlocal effective interaction $V(\mathbf{k}_1,\mathbf{k}_2;\mathbf{k}'_1,\mathbf{k}'_2)$ is considered. The momenta $\mathbf{k}_1$ and $\mathbf{k}_2$ are expressed as $\mathbf{k}_1 = \mathbf{k}_{\text{rel}} + \mathbf{q}_{\text{c.m.}}/2$ and $\mathbf{k}_2 = -\mathbf{k}_{\text{rel}} + \mathbf{q}_{\text{c.m.}}/2$ with the relative momentum $\mathbf{k}_{\text{rel}} = (\mathbf{k}_1 - \mathbf{k}_2)/2$ and the center-of-mass (c.m.) momentum $\mathbf{q}_{\text{c.m.}} = \mathbf{k}_1 + \mathbf{k}_2$.

In translationally invariant systems carrying no current, the paired state with $\mathbf{q}_{\text{c.m.}} = 0$ has the largest binding energy, and the interaction can be simplified to

$$V(\mathbf{k}_{\text{rel}}, -\mathbf{k}_{\text{rel}}; \mathbf{k}'_{\text{rel}}, -\mathbf{k}'_{\text{rel}}) \equiv V_{\text{rel}}(\mathbf{k}_{\text{rel}}, \mathbf{k}'_{\text{rel}}). \tag{8}$$

Only the s-wave part $V^{(0)}_{\text{rel}}(k_{\text{rel}}, k'_{\text{rel}})$ of $V_{\text{rel}}(\mathbf{k}_{\text{rel}}, \mathbf{k}'_{\text{rel}})$ can be retained in the low-momentum region [31].

The separable approximation for $V^{(0)}_{\text{rel}}(k_{\text{rel}}, k'_{\text{rel}})$ has been successfully applied to various nuclear systems [32–45]. In the present study, the Yamaguchi-type potential [45]

$$V^{(0)}_{\text{rel}}(k_{\text{rel}}, k'_{\text{rel}}) = -\gamma(k_{\text{rel}})\gamma(k'_{\text{rel}}) \tag{9}$$

with

$$\gamma(k_{\text{rel}}) = \frac{u}{k_{\text{rel}}^2 + \Lambda^2} \tag{10}$$

is adopted. Recently, the Yamaguchi-type potential was successfully applied to superfluid phase transitions of asymmetric nuclear matter [44]. The adopted parameters of $u = 2.6683$ MeV$^{-1/2}$ fm^{-2} and $\Lambda = 1.1392$ fm^{-1} were determined by the scattering length and the effective range of the $^1S_0$ nn scattering.

In the Borromean nuclei, a neutron pair is localized around the core nucleus, and it is necessary to take the $\mathbf{q}_{\text{c.m.}}$ dependence into the effective interaction. I assume a separable form,

$$V(\mathbf{k}_1,\mathbf{k}_2;\mathbf{k}'_1,\mathbf{k}'_2) = -\gamma(k_{\text{rel}})\eta(q_{\text{c.m.}})\gamma(k'_{\text{rel}})\eta(q'_{\text{c.m.}}). \tag{11}$$

The Gaussian-type form factor

$$\eta(q_{\text{c.m.}}) = (\sqrt{\pi}q_0)^{-3}e^{-(q_{\text{c.m.}}/q_0)^2} \tag{12}$$

is considered to have a role similar to the Gaussian-type effective core-n-n three-body interaction in real space [46–49]. The assumption of Eq. (11) should be justified by actually application in the present study.

The parameter $q_0 = 0.3588$ fm^{-1} is fixed by the experimental value of the $2n$ separation energy of $S_{2n} = 0.369$ MeV in ^{11}Li [50]. The choice of $q_0 = 0.3588$ fm^{-1} represents that the $2n$ correlations occur in the low-momentum neutron-halo region, namely, the surface-type interaction (see discussions of Figs. 3 and 9).

TABLE I. (a) Ground-state properties of ^{11}Li and ^{6}He. The kSEP interaction with $E_{\rm cut} = 100$ MeV and $q_0 = 0.3588$ fm^{-1} is used. The $2n$ separation energy, the fraction of the neutron $(s_{1/2})^2$, $(p_{1/2})^2$, and $(p_{3/2})^2$ configurations, the fraction of the $S = 0$ component, the core-$2n$ and n-n distances, and the matter radius are listed. (b) Same as (a) but $E_{\rm cut} = 120$ MeV and $q_0 = 0.3610$ fm^{-1} are used.

	S_{2n} (MeV)	$(s_{1/2})^2$ (%)	$(p_{1/2})^2$ (%)	$(p_{3/2})^2$ (%)	$S = 0$ (%)	$\bar{r}_{c\text{-}2n}$ (fm)	$\bar{r}_{nn}$ (fm)	R_m (fm)
	(a) $E_{\rm cut} = 100$ MeV and $q_0 = 0.3588$ fm^{-1}							
^{11}Li	0.369	27.1	59.0	1.4	60.7	5.00	6.78	3.20
^{6}He	0.980	5.0	15.5	72.9	96.8	4.07	5.14	2.70
	(b) $E_{\rm cut} = 120$ MeV and $q_0 = 0.3610$ fm^{-1}							
^{11}Li	0.369	26.9	59.2	1.4	60.7	4.98	6.76	3.19
^{6}He	0.994	4.9	15.6	72.9	96.8	4.05	5.13	2.70

Hereafter, the separable interaction in momentum space of Eq. (11) is abbreviated as the kSEP interaction for simplicity.

IV. APPLICATION TO ^{11}Li AND ^{6}He

^{11}Li and ^{6}He are Borromean nuclei in which the p-wave one-particle resonant states play a role. Numerous experimental and theoretical studies have been conducted on these nuclei (e.g., Ref. [7] for a recent review). In the present study, I do not intend to perform a comprehensive investigation, but I demonstrate the descriptive power of the three-body model using the kSEP interaction by comparing with the typical previous studies.

The single-particle Schrödinger equation of Eq. (2) is solved in k-space grids from zero to 2.5 fm^{-1} in steps of 0.08 fm^{-1}. The finer step of 0.045 fm^{-1} is also used for plotting dineutron structure such as the $2n$ density distribution. The orbital angular momenta $\ell \leqslant 9$ are considered. The cutoff energy is $E_{\rm cut} = 100$ MeV.

Table I (a) shows the ground-state properties of ^{11}Li and ^{6}He obtained by using $E_{\rm cut} = 100$ MeV and $q_0 = 0.3588$ fm^{-1}. (They are shown to check the convergence. The physical consideration will be given later.) If the cutoff energy is increased to $E_{\rm cut} = 120$ MeV, while the same value of $q_0 = 0.3588$ fm^{-1} is used, the $2n$ separation energy changes from 0.369 to 0.436 MeV for ^{11}Li (0.980 to 1.079 MeV for ^{6}He). This non-negligible $E_{\rm cut}$ dependence is due to the Lorentzian form for $k_{\rm rel}$ in the kSEP interaction.

The $E_{\rm cut}$ dependence is practically eliminated by tuning q_0 for each $E_{\rm cut}$. Table I (b) shows the result for ^{11}Li and ^{6}He using $E_{\rm cut} = 120$ MeV and $q_0 = 0.3610$ fm^{-1}, which is fixed by the experimental value of $S_{2n} = 0.369$ MeV in ^{11}Li. Compared to the result of $E_{\rm cut} = 100$ MeV, the change of S_{2n} in ^{6}He is 0.014 MeV, and the other quantities match with high accuracy.

A. Ground-state properties of ^{11}Li

For ^{11}Li, the ^{10}Li-n potential of Ref. [26] is adopted. The parameters are summarized in Table II. This potential reproduces the energy of the $p_{1/2}$ resonant state at 0.538 MeV [51]. The s-wave scattering length is $a_0 = -5.6$ fm.

TABLE II. Parameter sets of the core-n potential for ^{11}Li, ^{6}He, ^{22}C (C1 and C2), and ^{19}B. The single-particle angular-momentum quantum numbers $(l\,j)$, the strength parameter V_0 for the $(l\,j)$ state, the s-wave scattering length a_0, and the resonance energy E_R for the $(l\,j)$ state are listed. See text for details.

	r_0 (fm)	a_{cn} (fm)	f_{ls}	$l\,j$	V_0 (MeV)	$l\,j$	a_0 (fm)	E_R (MeV)
^{11}Li	1.27	0.67	1.006	ℓ = even	−47.5	$s_{1/2}$	−5.6	
				ℓ = odd	−35.366	$p_{1/2}$		0.538
^{6}He	1.25	0.65	0.93	$s_{1/2}$	−56.89			
				$p_{1/2}$	−68.53	$p_{1/2}$		1.27
				$j > 1/2$	−48.27	$p_{3/2}$		0.798
^{22}C	1.25	0.65	0.826	$s_{1/2}$	−29.80	$s_{1/2}$	−2.8	
(C1)				$\ell > 0$	−45.14	$d_{3/2}$		0.9
^{22}C	1.25	0.65	0.278	$s_{1/2}$	−29.80	$s_{1/2}$	−2.8	
(C2)				$\ell > 0$	−35.28	$d_{3/2}$		2.6
						$d_{5/2}$		1.5
^{19}B	1.25	0.65	0.826	$s_{1/2}$	−36.36	$s_{1/2}$	−50	
				$\ell > 0$	−37.43	$d_{3/2}$		1.37

The ground-state properties of ^{11}Li are shown in Table I (a). The weights of the neutron $(s_{1/2})^2$, $(p_{1/2})^2$, and $(p_{3/2})^2$ configurations are $P[(s_{1/2})^2] = 27.1\%$, $P[(p_{1/2})^2] = 59.0\%$, and $P[(p_{3/2})^2] = 1.4\%$, respectively. For the p states, it is close to the value of $P[(p_{1/2})^2] + P[(p_{3/2})^2] = 59 \pm 1\%$ in a recent knockout-reaction experiment [17]. For the s state, it is smaller than $P[(s_{1/2})^2] = 35 \pm 4\%$ of the same experiment. The authors of Ref. [52] pointed out that the weights of the s and p states have a model dependence in their extraction, and the same experimental data was best reproduced by equal weight ($\approx$48%) for the s and p states.

The determination of the weights is still under debate. For example, $P[(s_{1/2})^2]$ and the s-wave scattering length are 23% and −5.6 fm in the three-body model using the density-dependent contact interaction [25,26], 44% and −45.0 fm in the coupled-channel model [53], 47% and −17.4 fm in the tensor optimized shell model using bare interaction [54], 67% and −29.8 fm in the transfer to the continuum reaction framework (potential P3) [55].

The small $P[(s_{1/2})^2]$ is accompanied by the small negative value of a_0 in the shell-model-type calculations of Refs. [25,26] and the present study. As pointed out in Ref. [56], the coupling to the nonresonant continuum states with high orbital-angular-momentum ℓ is considered for the description of the dineutron correlation in the calculations. For example, I adopt the ^{10}Li-n potential of $a_0 = -5.6$ fm [25,26], and the admixture of the high-ℓ states up to $\ell \leqslant 9$ describes the dineutron structure, in spite of the small s-wave weight of 27%.

The core-$2n$ distance of 5.00 fm is consistent with the experimental values ranging from 5.01(32) [8] to 6.2(5) fm [4]. The n-n distance of 6.78 fm is in agreement with the extracted value of 6.6 ± 1.4 fm in the three-body correlation study of the dissociation of two neutrons [15] (see also Refs. [7,57] for the experimental value). The matter radius of 3.20 fm also fits into the range of the experimental values from 3.12(16) [58] to 3.71(20) fm [59]. Here, the observed matter radius of 2.32 fm in ^{9}Li [58] is used for the core radius parameter R_c in Eq. (7).

B. Ground-state properties of ^{6}He

For ^{6}He, the ^{4}He-n potential of Woods-Saxon type was constructed in Ref. [26]. This potential reproduces the low-energy ^{4}He-n phase shift, and the ^{4}He-n elastic scattering cross section is dominated by a peak of the $p_{3/2}$ resonance around 0.9 MeV. It was pointed out that the effective nn interaction has to be modified so as to reproduce the experimental value of $S_{2n} = 0.975$ MeV [60] in the three-body calculation using this ^{4}He-n potential and the density-dependent contact nn interaction. I also obtain the small value of $S_{2n} = 0.309$ MeV by using the same ^{4}He-n potential and the kSEP interaction.

In the present study, I reconstruct the ^{4}He-n potential of Ref. [26] by considering the updated experimental information. The parameters are summarized in Table II. The strength parameters of -48.27 and -65.14 MeV are fixed so as to reproduce the observed values of 0.798 MeV for the $p_{3/2}$ resonance energy and 2.068 MeV for the $p_{1/2}$ resonance energy [61], respectively.

For the s state, the strength parameter of -56.89 MeV is fixed for $P[(s_{1/2})^2] = 5\%$, a value which is similar to the observation with large uncertainty [62]. The admixture of a level of 5–10% was theoretical predicted (see, e.g., Refs. [47,63]). For the other (lj) states, the same strength parameter as the $p_{3/2}$ state is used. (If the strength parameter for the $p_{3/2}$ state is also used for the s state, $P[(s_{1/2})^2] = 3.7\%$ and $S_{2n} = 0.967$ MeV are obtained.)

The ground-state properties of ^{6}He are summarized in Table I. The value of $S_{2n} = 0.980$ MeV is in agreement with the experimental value of 0.975 MeV [60].

The weights of the $p_{3/2}$ and $p_{1/2}$ states are 72.9% and 15.5%, respectively. Because the energies of the $p_{3/2}$ and $p_{1/2}$ resonant states are fixed in the ^{4}He-n potential, the weight of the $p_{3/2}$ state becomes smaller while that for the $p_{1/2}$ state is larger, compared to those in the previous studies using the potential reproducing the ^{4}He-n phase shift. For example, $P[(s_{3/2})^2] = 83.0\%$ was obtained by the three-body calculation using the density-dependent contact nn interaction [25,26]. A recent three-body calculation with finite-range interactions gave $P[(p_{3/2})^2] = 87.5\%$ and $P[(p_{1/2})^2] = 3.7\%$ [47], although the sum of 91.1% is close to 88.4% in the present calculation. $P[(p_{1/2})^2] \approx 7\%$ was obtained by an analysis based the interference between the $p_{1/2}$ and $p_{3/2}$ states for the angular correlation of halo neutrons in the peripheral fragmentation of ^{6}He [64].

The core-$2n$ distance is 4.07 fm, which is consistent with the recent experimental value of 3.9(2) fm [10]. The n-n distance of 5.14 fm is within the uncertainty of the observed value of 5.9 ± 1.2 fm [15].

The matter radius of 2.70 fm is estimated by Eq. (7) using the radius of 1.462 fm of ^{4}He deduced from the charge-radius measurement [65]. This value of the matter radius fits the range of the available experimental data from 2.33 ± 0.04 fm [66] to 2.71 ± 0.04 fm [67]. Here, the small value of 2.33 ± 0.04 fm [66] was obtained by the analysis of the static density (optical limit) Glauber model for the interaction cross section of $\sigma = 722 \pm 5$ mb [66], while the large value of 2.71 ± 0.04 fm [67] (2.54 ± 0.04 fm [68]) was obtained from the same experimental data but by considering the few-body correlations based on the zero-range (finite-range) Faddeev wave function model.

V. TWO-NEUTRON CORRELATIONS IN ^{11}Li AND ^{6}He

A. Two-neutron density for ^{11}Li

I show the $2n$ density for ^{11}Li to see the spatial correlation of valence neutrons. The total $2n$ density can be decomposed into the $S = 0$ and $S = 1$ components in the LS-coupling scheme. ("Total" emphasizes the sum of the S components.) For the spherical core-n potential, the $2n$ density in real space can be expressed as $\rho_2(r_1, r_2, \theta_r)$ using the radial coordinates r_1 and r_2 and the opening angle between them, θ_r [1,25]. In the same manner, the $2n$ density in momentum space can be expressed as $\rho_2(k_1, k_2, \theta_k)$ using $k_1 = |\mathbf{k}_1|$, $k_2 = |\mathbf{k}_2|$, and the opening angle between them, θ_k. Note that $\rho_2(k_1, k_2, \theta_k)$ is normalized as

$$\int_0^\infty 4\pi k_1^2 dk_1 \int_0^\infty k_2^2 dk_2 \times \int_0^\pi 2\pi \sin\theta_k d\theta_k \rho_2(k_1, k_2, \theta_k) = 1. \tag{13}$$

Figures 1(a) and 1(b) show the total $2n$ density and the $S = 0$ component for ^{11}Li as functions of $r = r_1 = r_2$ and θ_r. Here, it is weighted with $8\pi^2 r^4 \sin\theta_r$.

As pointed out by several authors (e.g., Ref. [25]), there are two peaks, and the asymmetric angular distribution is caused by the interference of the different-parity s and $p_{1/2}$ states. The higher peak at $(r, \theta_r) = (3.5\ \text{fm}, 26^\circ)$ corresponds to the dineutron configuration, and it has a long r tail for the halo structure. The narrow angular distribution indicates the short n-n distance.

The lower peak at $(r, \theta_r) = (2.8\ \text{fm}, 106^\circ)$ corresponds to the cigarlike configuration. The peak is rather compact in the r direction, while the angular distribution is wider, compared to the dineutron configuration.

Figures 2(a) and 2(b) show the total $2n$ density (and the $S = 0$ component) for ^{11}Li as functions of $k_n = k_1 = k_2$ and θ_k. It is weighted with $8\pi^2 k_n^4 \sin\theta_k$. The peak for the dineutron configuration appears at the low momentum of $(k_n, \theta_k) = (0.18\ \text{fm}^{-1}, 128^\circ)$ for the halo structure. It is accompanied by a broad angular distribution, contrary to the narrow angular distribution in real space. The peak for the dineutron configuration has a long k_n tail, which indicates the strong dineutron correlation [see the discussion of Fig. 3(b)]. The peak for the cigarlike configuration appears at the higher momentum of $(k_n, \theta_k) = (0.40\ \text{fm}^{-1}, 78^\circ)$.

I also consider the dineutron structure by associating with the c.m. momentum $q_{\text{c.m.}}$. This is because an opening angle θ_k for a given k_n contains various $q_{\text{c.m.}}$ components representing different neutron-pair structures. I define the c.m. density $\rho_{\text{c.m.}}$ and the RMS core-n momentum $\bar{k}_n$ of valence neutrons as a

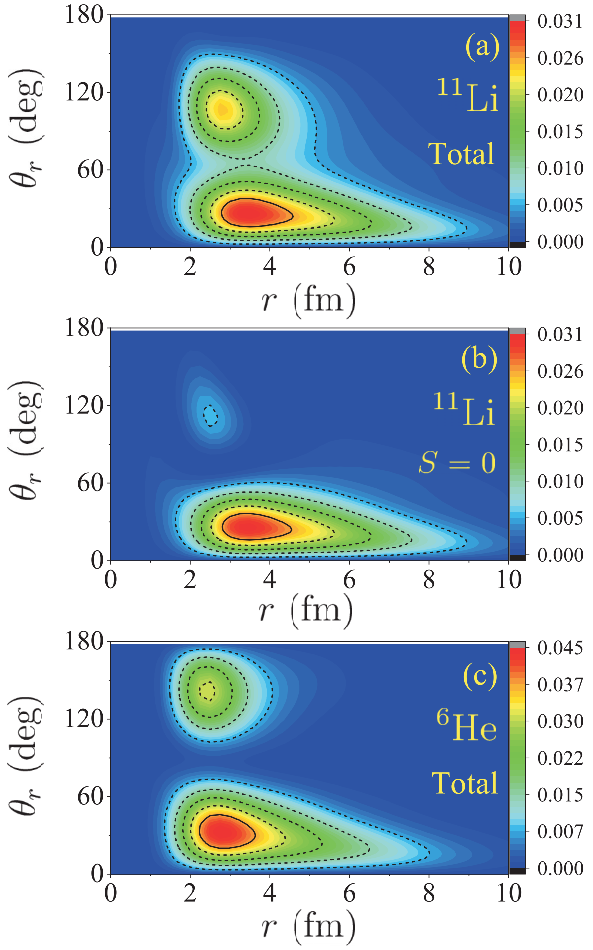

FIG. 1. (a) Total $2n$ density for ^{11}Li as functions of $r_1 = r_2 = r$ and the angle between the valence neutrons, θ_r. It is weighted with a factor of $8\pi^2 r^4 \sin\theta_r$. The peak for the dineutron configuration is indicated by the red (dark gray) region inside the solid contour line. (b) Same as (a) but for the $S = 0$ component of ^{11}Li. (c) Same as (a) but for the total $2n$ density of ^{6}He.

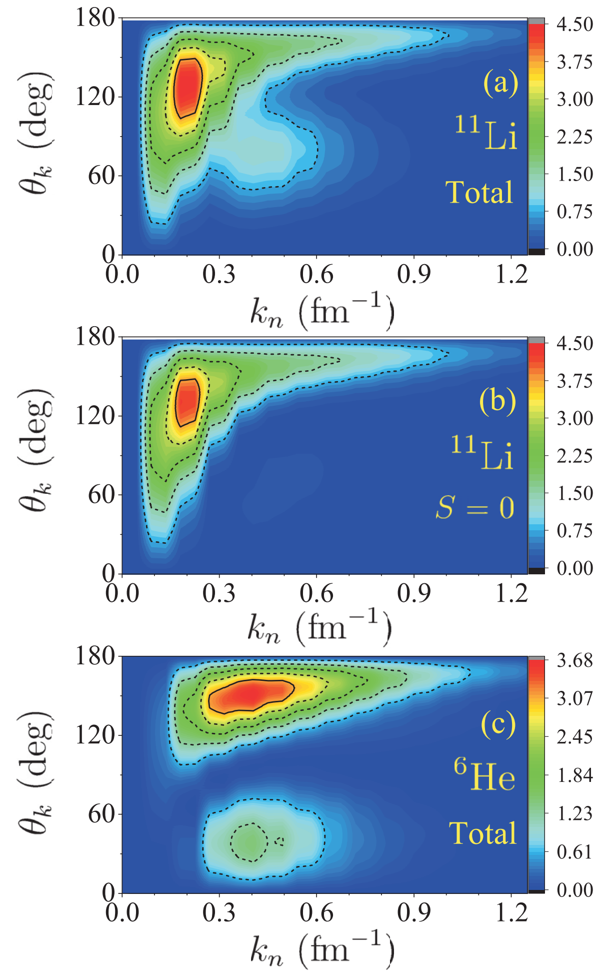

FIG. 2. (a) Total $2n$ density for ^{11}Li as functions of $k_1 = k_2 = k_n$ and the angle between the valence neutrons, θ_k. It is weighted with a factor of $8\pi k_n^4 \sin\theta_k$. The peak for the dineutron configuration is indicated by the red (dark gray) region inside the solid contour line. (b) Same as (a) but for the $S = 0$ component of ^{11}Li. (c) Same as (a) but for the total $2n$ density of ^{6}He.

function of $q_{\text{c.m.}}$ by

$$\rho_{\text{c.m.}}(q_{\text{c.m.}}) = \int d^3k_1 d^3k_2\, \rho_2(\mathbf{k}_1, \mathbf{k}_2)\, \delta(q_{\text{c.m.}} - |\mathbf{q}_{\text{c.m.}}|), \tag{14}$$

and

$$[\bar{k}_n(q_{\text{c.m.}})]^2 = \frac{1}{\rho_{\text{c.m.}}(q_{\text{c.m.}})} \int d^3k_1 d^3k_2\, (\mathbf{k}_1)^2\, \rho_2(\mathbf{k}_1, \mathbf{k}_2) \times \delta(q_{\text{c.m.}} - |\mathbf{q}_{\text{c.m.}}|). \tag{15}$$

Here, $\mathbf{q}_{\text{c.m.}} = \mathbf{k}_1 + \mathbf{k}_2$, and $\rho_{\text{c.m.}}$ is normalized as $\int_0^\infty \rho_{\text{c.m.}}(q_{\text{c.m.}}) dq_{\text{c.m.}} = 1$. The same quantities but for the $S = 0$ component are calculated in the same manner.

Figure 3(a) shows the c.m. density obtained from the total $2n$ density of ^{11}Li. The peak component appears from zero to $q_{\text{c.m.}} \approx 0.4$ fm^{-1}. The choice of $q_0 = 0.3588$ fm^{-1} for the kSEP interaction represents that the $2n$ correlations occur around the low-$q_{\text{c.m.}}$ peak of halo neutrons, namely, the surface-type interaction. The peak at $q_{\text{c.m.}} \approx 0.2$ fm^{-1} corresponds to the peak at $k_n \approx 0.2$ fm^{-1} for the dineutron configuration in the $2n$ density [see Fig. 2(a)]. The cigarlike configuration appears above $q_{\text{c.m.}} \approx 0.2$ fm^{-1}.

Figure 3(b) shows the RMS core-n momentum for ^{11}Li. The local maximum value of $\bar{k}_n$ for the total $2n$ density is 0.62 fm^{-1} at $q_{\text{c.m.}} = 0.43$ fm^{-1}. It determines not only the peak region of $\rho_{\text{c.m.}}$ but also the k_n region covering the peaks of the dineutron and cigarlike configurations [see Fig. 2(a)]. Here, I refer to the local maximum value of $\bar{k}_n$ for the total $2n$ density as the surface momentum k_{surf}. The region of $k_n < k_{\text{surf}}$ is interpreted as the low-momentum neutron-halo region in the Borromean nuclei.

The local maximum value of $\bar{k}_n$ for the $S = 0$ component is 0.86 fm^{-1} at $q_{\text{c.m.}} = 0.52$ fm^{-1}. It determines the long k_n-tail distribution of the $2n$ density [see Fig. 2(b)]. The associated large opening angle, $\theta_{\text{tail}} = 2\cos^{-1}[(q_{\text{c.m.}}/2)/\bar{k}_n] = 145°$, indicates the strong dineutron correlation. [See the inset of Fig. 3(b) for the definition of θ_{tail}.]

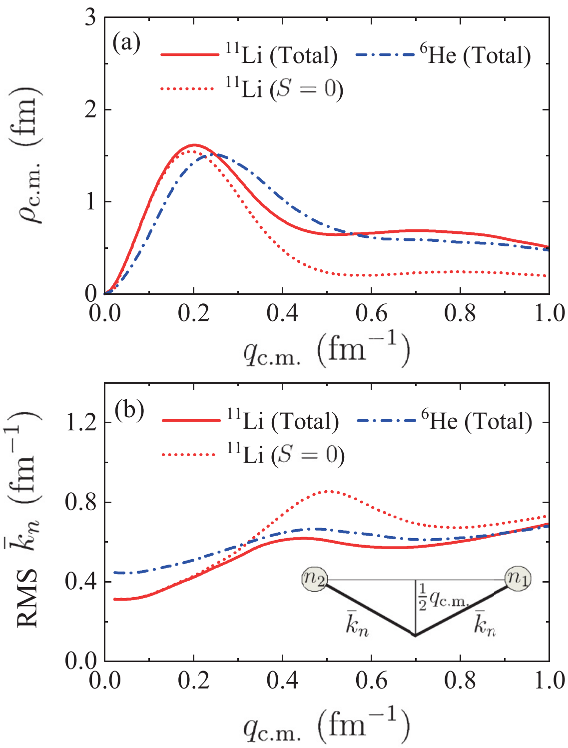

FIG. 3. (a) Plot for the c.m. density distribution $\rho_{\text{c.m.}}$ of ^{11}Li (total $2n$ density and the $S = 0$ component) and ^{6}He (total $2n$ density) as a function of $q_{\text{c.m.}}$. (b) Same as (a) but for the RMS core-n momentum $\bar{k}_n$. See text for details.

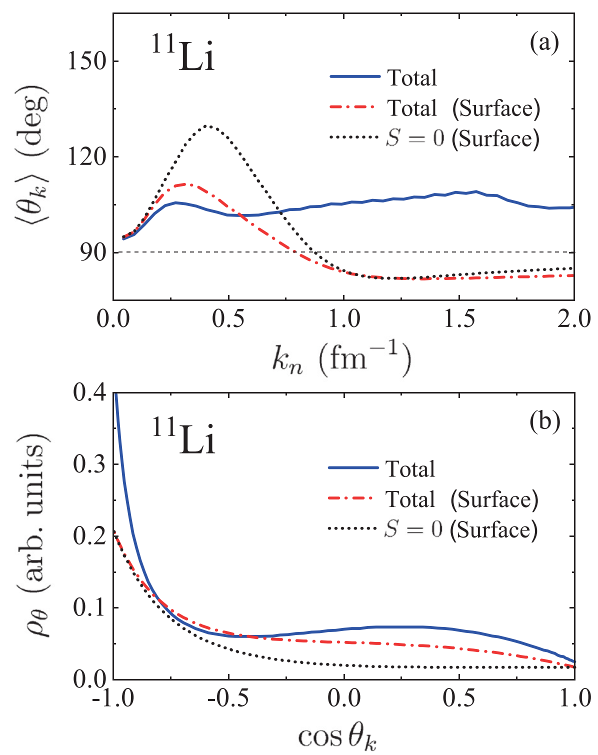

FIG. 4. (a) Mean opening angle $\langle\theta_k\rangle$ as a function of k_n for ^{11}Li (total $2n$ density and the $S = 0$ component). "Surface" indicates the result imposing the cutoff $k_{\text{cut}} = k_{\text{surf}}$. (b) Same as (a) but for the opening-angle distribution ρ_θ as a function of $\cos\theta_k$.

B. Angular correlations in ^{11}Li

The angular correlations in peripheral fragmentation of the Borromean nuclei can provide information on the spatial structure of the dineuton. Measurements using the one-neutron knockout reaction have been done for ^{11}Li [17,69,70], ^{6}He [64,71], and ^{14}Be [70]. The fragmentation process is dominated by a sequential mechanism. One neutron is first knocked out while the rest of the system remains essentially untouched. The residual unbound two-body system subsequently decays into a neutron and a charged fragment (see, e.g., Refs. [64,69,71]).

Recently, the mean correlation angle $\langle\theta_{nf}\rangle$ between momenta of emitted neutrons n_1 and n_2 in the reaction channel $^{11}\text{Li}(p, pn_1)\,^{10}\text{Li}^* \rightarrow {}^{9}\text{Li} + n_2$ was measured as a function of the missing momentum k of n_1 [17]. The correlation angle θ_{nf} is defined in the Jacobi coordinate (e.g., Refs. [64,69]), and θ_k and θ_{nf} coincide with each other in the large-A_c Borromean nuclei. The observed $\langle\theta_{nf}\rangle$ shows a clear k dependence. $\langle\theta_{nf}\rangle$ has a maximum value of about 100° at $k \approx 0.3$ fm^{-1}, and it decreases at smaller and larger k values. At $k \approx 0$, $\langle\theta_{nf}\rangle$ is close to the uncorrelated limit of 90°. Above $k \approx 0.9$ fm^{-1}, there is a plateau of $\langle\theta_{nf}\rangle \approx 87°$, which is also close to 90°.

In the present study, I clarify how the mean opening angle $\langle\theta_k\rangle$ reflects the $2n$ density distribution. The similarities between $\langle\theta_k\rangle$ and $\langle\theta_{nf}\rangle$ are indicated, although one should be careful with a direct comparison due to the uncertainties of the final-state interactions and the optical potentials in the analysis [47,52].

I define $\langle\theta_k\rangle$ as a function of k_n by

$$\cos\langle\theta_k\rangle \equiv \left[\int_0^{k_{\text{cut}}} k_2^2 dk_2 \int_0^{\pi} 2\pi \sin\theta_k d\theta_k \times \rho_2(k_n, k_2, \theta_k)\cos\theta_k\right] \Big/ \rho_k(k_n) \tag{16}$$

with one-neutron density distribution

$$\rho_k(k_n) = \int_0^{k_{\text{cut}}} k_2^2 dk_2 \int_0^{\pi} 2\pi \sin\theta_k d\theta_k \times \rho_2(k_n, k_2, \theta_k). \tag{17}$$

Here, k_{cut} is a cutoff momentum. I examine two cases of $k_{\text{cut}} = k_{\text{surf}}$ and $k_{\text{cut}} = \infty$ (no cutoff). $\langle\theta_k\rangle$ for the $S = 0$ component is also defined in the same manner.

Figure 4(a) shows $\langle\theta_k\rangle$ of ^{11}Li. $\langle\theta_k\rangle$ (no cutoff) has a maximum value of 105° at $k_n = 0.27$ fm^{-1}. It decreases at lower and larger k_n value, but it gradually increases above $k_n \approx 0.5$ fm^{-1}, contrary to the observed $\langle\theta_{nf}\rangle$. $\langle\theta_k\rangle$ decreases again above $k_n \approx 1.5$ fm^{-1} due to the low one-neutron density (see Fig. 5).

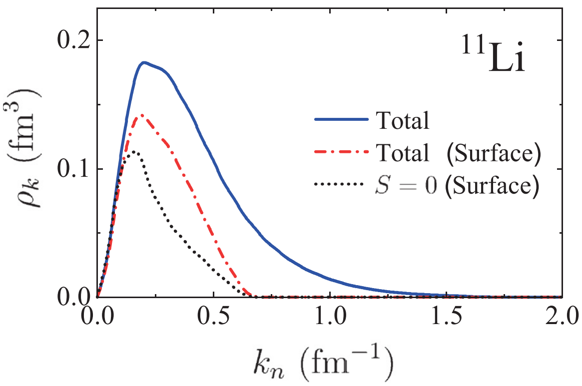

FIG. 5. Same as Fig. 4(a) but for the one-neutron density distribution of ^{11}Li.

The authors of Ref. [52] pointed out that the mean correlation angle at high missing momentum strongly depends on the absorption effects at the small distance between the proton target and the ^{9}Li core. Eventually, the collision between the proton target and the valence neutron takes place at a large distance from the ^{9}Li core, and the absorptive effect for the halo neutron was expected to be small.

Within my model, I examine the influence of the cutoff $k_{\rm cut} = k_{\rm surf}$, which indicates that the only halo neutrons contribute to $\langle\theta_k\rangle$. The value of $k_{\rm cut}$ can be changed according to the experimental conditions, but I examine only $k_{\rm cut} = k_{\rm surf}$ for the qualitative discussion.

Figure 4(a) shows $\langle\theta_k\rangle$ for the total $2n$ density imposing $k_{\rm cut} = k_{\rm surf}$. $\langle\theta_k\rangle$ has a maximum value of 111° at $k_n = 0.31$ fm^{-1}. It decreases at smaller and larger k_n values. At $k_n \approx 0$, it approaches to around 90°. Above $k_n \approx 1.0$ fm^{-1}, there is a plateau of $\langle\theta_k\rangle \approx 82^\circ$.

To understand the k_n dependence, Fig. 5 shows the one-neutron density imposing $k_{\rm cut} = k_{\rm surf}$. The distributions with and without the cutoff coincide with each other from zero to $k_n \approx 0.14$ fm^{-1}. The influence of the cutoff is already noticeable at the peak position of $k_n = 0.18$ fm^{-1}. Above $k_n = k_{\rm surf}$, the one-neutron density imposing $k_{\rm cut} = k_{\rm surf}$ is very low, and $\langle\theta_k\rangle$ becomes independent of k_n.

The characteristic k_n dependence of $\langle\theta_k\rangle$ is close to the missing momentum k dependence of the observed $\langle\theta_{nf}\rangle$, although the reaction mechanize is not considered, except for the cutoff $k_{\rm cut} = k_{\rm surf}$.

Figure 4(a) also shows $\langle\theta_k\rangle$ for the $S = 0$ component imposing $k_{\rm cut} = k_{\rm surf}$. The maximum has a higher value of 130° at $k_n = 0.41$ fm^{-1}. This is due to the absence of the cigarlike configuration with smaller θ_k. The k_n dependence of the one-neutron density for the $S = 0$ component shown in Fig. 5 can be also understood by the absence of the cigarlike configuration around $k_n = 0.4$ fm^{-1} [see Fig. 2(a)].

The asymmetric correlation-angle distribution between the knockout neutron and the one from the decay of ^{10}Li was measured in the fragment-neutron coincidence experiment [69]. The correlation-angle distribution was well approximated by a polynomial expansion of $d\sigma/d\cos(\theta_{nf}) \approx \mathcal{W}(\theta_{nf}) = 1 - 1.03(4)\cos\theta_{nf} + 1.41(8)\cos^2\theta_{nf}$ [69].

In connection with the observation, I define the opening-angle distribution $\rho_\theta(\theta_k)$ for the $2n$ density as

$$\rho_\theta(\theta_k) = N_\theta \int_0^{k_{\rm cut}} 4\pi k_1^2 dk_1 \int_0^{k_{\rm cut}} k_2^2 dk_2 \rho_2(k_1, k_2, \theta_k). \quad (18)$$

The opening-angle distribution for the $S = 0$ component is also defined in the same manner. N_θ is an arbitrarily chosen normalization factor for better display.

Figure 4(a) shows the opening-angle distribution (no cutoff) of the total $2n$ density using $N_\theta = 1$. The distribution shows the large asymmetry. The ratio $\rho_\theta(180^\circ)/\rho_\theta(90^\circ) = 6.58$ is about 1.9 times larger than the experimental estimation of $\mathcal{W}(180^\circ)/\mathcal{W}(90^\circ) = 3.44$.

I also show the opening-angle distribution imposing $k_{\rm cut} = k_{\rm surf}$. By considering the contribution of the only halo neutrons, the ration becomes 4.03, which is only 17% deviation from the experimental value. The experimental ratio of 3.44 also indicates the contribution of the cigarlike configuration by comparing to the large value of $\rho_\theta(180^\circ)/\rho_\theta(90^\circ) = 10.5$ for the $S = 0$ component imposing $k_{\rm cut} = k_{\rm surf}$.

C. Angular correlations in ^{6}He

Figure 1(c) shows the total $2n$ density for ^{6}He as functions of $r = r_1 = r_2$ and θ_r. The plot for the $S = 0$ component is similar to the total $2n$ density due to the large $P[S = 0] = 96.8\%$. As pointed out in the previous studies (e.g., Ref. [7], and references therein), the ground state is mainly the admixture of the same-parity $p_{1/2}$ and $p_{3/2}$ states. The $2n$ density has two peaks at $(r, \theta_r) = (3.5$ fm, $26^\circ)$ and $(2.5$ fm, $112^\circ)$ for the dineutron and cigarlike configurations, respectively.

Figure 2(c) shows the total $2n$ density for ^{6}He as functions of $k_n = k_1 = k_2$ and θ_k. The two peaks appear at the similar k_n regions of $(k_n, \theta_k) = (0.40$ fm^{-1}, $152^\circ)$ and $(0.40$ fm^{-1}, $38^\circ)$ for the dineutron and cigarlike configurations, respectively.

Figures 3(a) and 3(b) show $\rho_{\rm c.m.}$ and $\bar{k}_n$ for the total $2n$ density of ^{6}He. The low-$q_{\rm c.m.}$ peak component below $q_{\rm c.m.} \approx 0.4$ fm^{-1} corresponds to the surface region where the $2n$ correlations occur. (It is consistent with the choice of $q_0 = 0.3588$ fm^{-1} for the kSEP interaction as the surface type.) Compared to ^{11}Li, the peak of $\rho_{\rm c.m.}$ shifts toward higher $q_{\rm c.m.}$, and the value of $\bar{k}_n$ is overall higher, as expected from the total $2n$ density [see Fig. 2(c)]. The local maximum value of $\bar{k}_n = 0.67$ fm^{-1} at $q_{\rm c.m.} = 0.47$ fm^{-1} is adopted as the surface momentum $k_{\rm surf}$.

The local maximum value of $\bar{k}_n$ for the $S = 0$ component is the same value of 0.67 fm^{-1}. It determines the long k_n-tail distribution of the $2n$ density. The associated large opening angle, $\theta_{\rm tail} = 2\cos^{-1}[(q_{\rm c.m.}/2)/\bar{k}_n] = 139^\circ$, indicates the strong dineutron correlation.

Figure 6(a) shows $\langle\theta_k\rangle$ for the total $2n$ density of ^{6}He. As in ^{11}Li, $\langle\theta_k\rangle$ (no cutoff) is almost constant, and it decreases above $k_n \approx 1.5$ fm^{-1} due to the low one-neutron density. $\langle\theta_k\rangle$ imposing $k_{\rm cut} = k_{\rm surf}$ has a maximum value of 108° at $k_n = 0.23$ fm^{-1}, and it decreases at smaller and larger k_n values. Above $k_n \approx 1.2$ fm^{-1}, $\langle\theta_k\rangle$ becomes constant around 86°.

Figure 6(b) shows the opening-angle distribution for the total $2n$ density of ^{6}He. The influence of the cutoff $k_{\rm cut} = k_{\rm surf}$ is small. The opening-angle distribution coincides well with

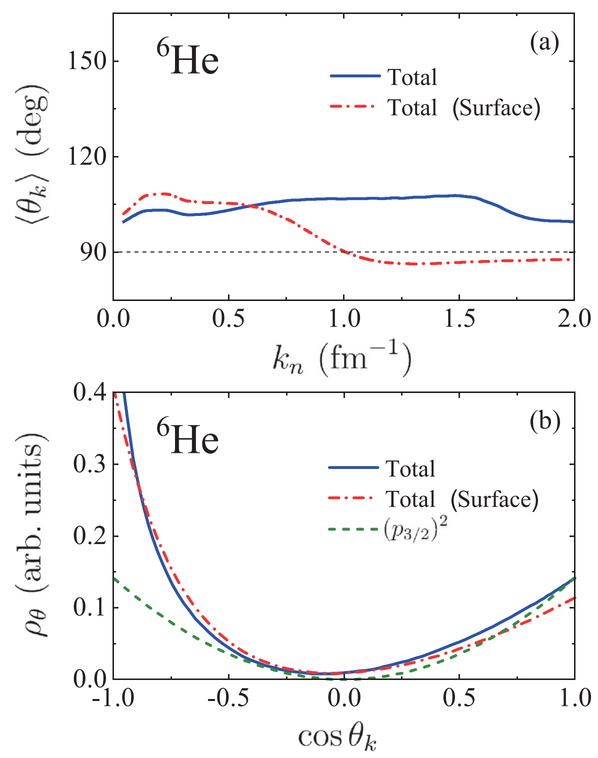

FIG. 6. Same as Fig. 4 but for ^{6}He. For comparison, the opening-angle distribution ρ_θ for the pure $(p_{3/2})^2$ configuration is shown.

the distribution of $\rho_\theta(\theta_k) \propto \cos^2\theta_k$ for the pure-$(p_{3/2})^2$ configuration (the same as $\cos^2\theta_r$ in the real space [25]), except for the large dineutron component at $\cos\theta_k < -0.5$.

Although the large dineutron component in the $2n$ density has been pointed out by several authors (e.g., Ref. [25]), the observed correlation-angle distribution is rather symmetric, $d\sigma/d\cos(\theta_{nf}) \approx 1 + 1.5\cos^2(\theta_{nf})$ [64]. This may be due to the difference of θ_k and θ_{nf}, which coincide with each other in the large-A_c Borromean nuclei. Actually, the rather symmetric correlation-angle distribution for the ground state of ^{6}He was shown in Ref. [47]. More quantitative analyses for extracting the dineutron structure from the observations remain for further studies.

VI. APPLICATION TO ^{22}C

I apply the three-body model using the kSEP force to the Borromean nuclei ^{22}C and ^{19}B in which the d-wave one-particle resonant states play a role. For ^{22}C, the observed values of S_{2n} with large uncertainties are 0.42 ± 0.96 MeV [72] and -0.14 ± 0.46 MeV ($S_{2n} < 0.32$ MeV) [73]. The significant neutron s-wave contribution in ^{22}C was suggested by the measurements of the large reaction cross section [74], the interaction cross section [75], and the momentum distribution of the neutron removal cross section [76]. The observed decay-energy spectrum in ^{21}C could be described with an s-wave virtual state of the scattering length $|a_0| < 2.8$ fm [77]. Previous theoretical studies also emphasized the large s-wave contribution [77–85].

However, the origin of the large s-wave contribution is still under debate. Here, the current situation is briefly summarized for justification of the three-body description of ^{22}C. The large s-wave contribution in the ground states of ^{19,20}C was also suggested by the observed momentum distributions of the neutron removal cross section [76]. The observed ground-state spin-parity of $I^\pi = 1/2^+$ in ^{19}C [86] is also in agreement with the interpretation that the 13th neutron is placed on the [211 1/2] one-particle state in the prolately deformed potential. It was pointed out in Ref. [87] that the s-wave component is dominant in the weakly bound [211 1/2] state.

The minor role of the s-wave component in the core nucleus ^{20}C of ^{21,22}C may be understood by considering a different shape from the ground state of ^{20}C. The unbound nucleus ^{21}C was not observed as a low-lying resonant state [77], and it is consistent with the ground-state spin-parity of $I^\pi = 1/2^+$. It was considered in Ref. [77] that the 15th neutron is placed on the s-wave virtual state assuming as spherical shape. In Ref. [87], the 15th neutron is consider to be in the [211 1/2] state in the potential with small oblate shape. In both interpretations, the 13th and 14th neutrons are placed on the $1d_{5/2}$ state or the [211 3/2] state in the core nucleus ^{20}C.

A. ^{20}C-n potential

Precise experimental information about the one-particle resonant states in ^{21}C is missing so far. Several studies suggested the low-lying $d_{3/2}$ state [88,89] and the $d_{5/2}$ state [76,90].

I examine the two parameter sets of C1 and C2 for the ^{20}C-n potential. The parameters are summarized in Table II. In both C1 and C2, $a_{cn} = 0.65$ fm and $r_0 = 1.25$ fm of Set 2 in Ref. [89] are used. For the s state, the strength parameter of -29.80 MeV is fixed by $a_0 = -2.8$ fm.

For C1, I consider the low-lying $d_{3/2}$ resonant state which was introduced to reproduce the observed values of the $2n$ separation energy and the matter radius [88,89]. The strength parameter of -45.14 MeV for the $\ell > 0$ states gives the $d_{3/2}$ resonant state at 0.9 MeV. Here, $f_{ls} = 0.826$ of Set 2 in Ref. [89] is used. Set C1 gives $S_{2n} = 0.111$ MeV, which is consistent with the experimental upper limit of $S_{2n} < 0.32$ MeV [73].

For C2, the two d resonant states are considered. The shell-model calculation using the WBP interaction predicted the $5/2^+$ and $3/2^+$ states at 1.11 and 2.19 MeV in ^{21}C, respectively [76]. The observed momentum distribution of the neutron removal cross section from ^{22}C was well reproduced by considering them as the $d_{5/2}$ and $d_{3/2}$ states [76].

A measurement by invariant mass spectroscopy of ^{21}C suggested that the resonant state at about 1.5 MeV may be identified as the $5/2^+$ state [90]. The strength parameter of -35.28 MeV for the $\ell > 0$ states gives the $d_{5/2}$ state at 1.5 MeV. $f_{ls} = 0.278$ is determined so as to give the same level spacing of 1.1 MeV between the $5/2^+$ and $3/2^+$ states in the shell model calculation [76]. Set C2 gives $S_{2n} = 0.202$ MeV, which is consistent with the upper limit of $S_{2n} < 0.32$ MeV [73].

TABLE III. Same as Table I but for ^{22}C (sets C1 and C2) and ^{19}B. The fractions of the neutron $(s_{1/2})^2$, $(d_{3/2})^2$, and $(d_{5/2})^2$ configurations are shown.

	S_{2n} (MeV)	$(s_{1/2})^2$ (%)	$(d_{3/2})^2$ (%)	$(d_{5/2})^2$ (%)	$S=0$ (%)	$\bar{r}_{c\text{-}2n}$ (fm)	$\bar{r}_{nn}$ (fm)	R_m (fm)
^{22}C (C1)	0.111	28.1	60.3	0.8	64.1	5.08	7.53	3.39
^{22}C (C2)	0.202	32.9	12.3	46.1	97.4	5.20	7.55	3.41
^{19}B	0.490	54.7	3.4	35.9	93.9	5.15	8.16	3.50

B. Ground-state properties of ^{22}C

The ground-state properties of ^{22}C are summarized in Table III. Both C1 and C2 give similar values of $\bar{r}_{c\text{-}2n}$ and $\bar{r}_{nn}$. The matter radius of C1 (C2) is 3.39 (3.41) fm, which is in agreement with the experimental value of 3.44 ± 0.08 fm [75]. Here, the matter radius of 2.98 fm in ^{20}C [58] is used for R_c in Eq. (7). For both C1 and C2, the weights of the configurations are about 30% for the s state and about 60% for the sum of the d states. Obviously, the $d_{3/2}$ ($d_{5/2}$) state has the largest weight of 60.3% (46.1%) for C1 (C2).

The fraction of the $S=0$ component is a small value of 64.1% for C1, while it is 97.4% for C2. It reflects the coefficients of the angular-momentum coupling in $\Psi^{(2)}_{n_1 n_2 l j}(\mathbf{k}_1, \mathbf{k}_2)$ of Eq. (5) (see the C coefficient in Eq. (A.5) of Ref. [1]). The influence of the $S=0$ and 1 components on the opening-angle distribution will be discussed in Sec. VI C.

C. Angular correlations in ^{22}C

Figures 7(a) and 7(b) show the real-space total $2n$ density and the $S=0$ component for ^{22}C (C1). As pointed out by the previous studies (e.g., Ref. [89], and references therein), there are three peaks at $(r, \theta_r) = (3.8\ \text{fm},\ 22^\circ)$, $(3.3\ \text{fm},\ 132^\circ)$, and $(3.3\ \text{fm},\ 66^\circ)$ for the dineutron, cigarlike, and boomerang configurations, respectively. The boomerang configuration appears due to the admixture of the d and f waves coupled to even L (see, e.g., Ref. [85]). The ground-state configuration is mainly the admixture of the same-parity s and d states. The interference with the p states of the 6.4% weight causes the large dineutron component [see also the discussion of the opening-angle distribution in Fig. 10(b)].

Figure 7(c) shows the real-space total $2n$ density for ^{22}C (C2). The plot for the $S=0$ component is almost the same due to $P[S=0] = 97.4\%$. The overall structure is also similar to that for the $S=0$ component of C1. The large dineutron component is caused by the interference with the p states of the 4.4% weight.

Figures 8(a) and 8(b) show the momentum-space total $2n$ density and the $S=0$ component for C1. The peak for the dineutron configuration appears at low momentum of $(k_n, \theta_k) = (0.14\ \text{fm}^{-1},\ 106^\circ)$, and the angular distribution is remarkably wide. The peaks for the cigarlike and boomerang configurations appear at higher momenta of $(k_n, \theta_k) = (0.68\ \text{fm}^{-1},\ 44^\circ)$ and $(0.72\ \text{fm}^{-1},\ 124^\circ)$, respectively.

Figure 8(c) shows the total $2n$ density for C2. The plot is similar to that of the $S=0$ component for C1. The peaks

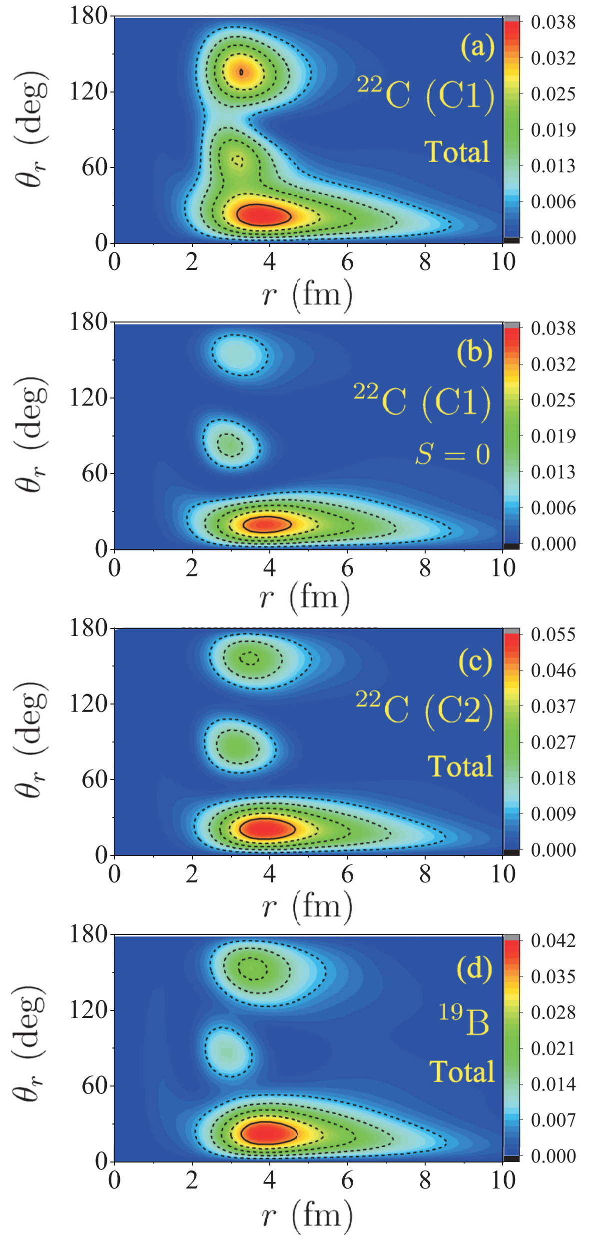

FIG. 7. Same as Fig. 1 but for ^{22}C (sets C1 and C2) and ^{19}B. The $S=0$ component for ^{22}C (C1) is also shown.

appear at $(k_n, \theta_k) = (0.14\ \text{fm}^{-1},\ 104^\circ)$, $(0.68\ \text{fm}^{-1},\ 24^\circ)$, and $(0.59\ \text{fm}^{-1},\ 96^\circ)$ for dineutron, cigarlike, and boomerang configurations, respectively. The peak of the dineutron configuration for C2 is 39% higher than that for C1 due to the larger low-q_{cm} component of the $2n$ density.

To see this, Fig. 9(a) shows $\rho_{\text{c.m.}}$ obtained from the total $2n$ densities of C1 and C2. The peak component from zero to $q_{\text{c.m.}} \approx 0.4\ \text{fm}^{-1}$ corresponds the surface region where the $2n$ correlations occur. (It is consistent with the choice of $q_0 = 0.3588\ \text{fm}^{-1}$ for the kSEP interaction as the surface type.) The low-$q_{\text{c.m.}}$ component for C2 is larger due to the larger s-wave weight and the higher d-wave resonance energies. For C1, $\rho_{\text{c.m.}}$ of the $S=0$ component is also shown. The $S=1$

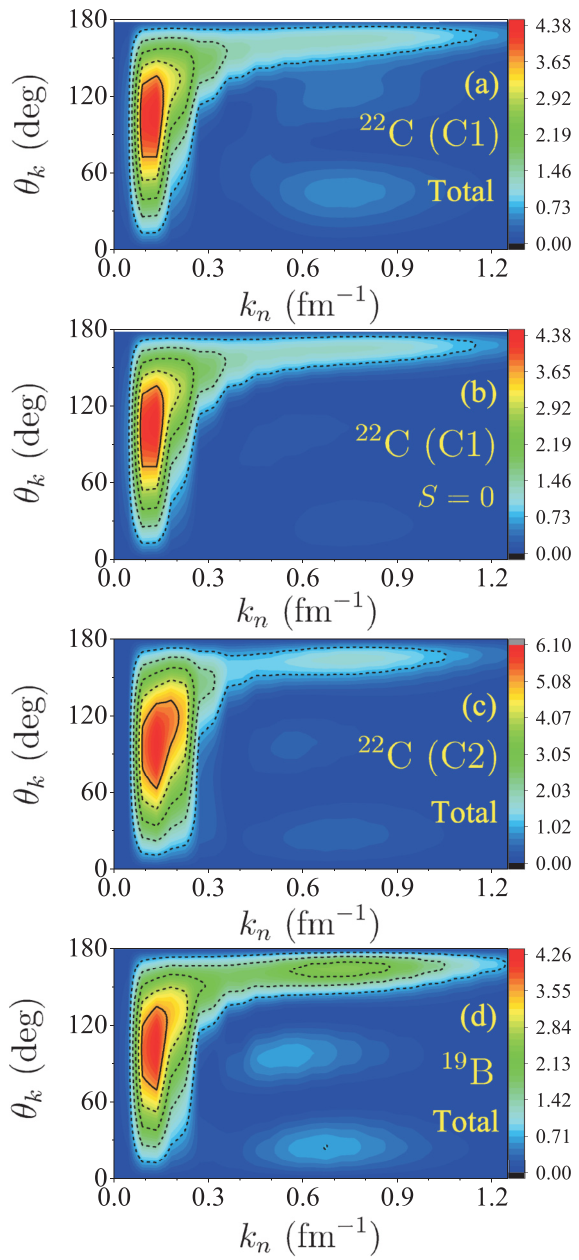

FIG. 8. Same as Fig. 2 but for ^{22}C (sets C1 and C2) and ^{19}B. The $S = 0$ component for ^{22}C (C1) is also shown.

component of the cigarlike and boomerang configurations appears above $q_{\mathrm{c.m.}} \approx 0.3$ fm^{-1}.

Figure 9(b) shows $\bar{k}_n$ for ^{22}C. For C1 (C2), the local maximum value of $\bar{k}_n = 0.87(0.89)$ fm^{-1} at $q_{\mathrm{c.m.}} = 0.43$ (0.43) fm^{-1} is adopted as the surface momentum k_{surf}.

The local maximum value of $\bar{k}_n$ for the $S = 0$ component is 0.96 (0.89) fm^{-1} at $q_{\mathrm{c.m.}} = 0.43$ (0.43) fm^{-1} for C1 (C2). It determines the long k_n-tail distribution of the $2n$ density [see Figs. 8(b) and 8(c)]. The associated large opening angle, $\theta_{\mathrm{tail}} = 2\cos^{-1}[(q_{\mathrm{c.m.}}/2)/\bar{k}_n] = 154^\circ(152^\circ)$, indicates the strong dineutron correlation.

Figure 10(a) shows $\langle\theta_k\rangle$ of the total $2n$ density imposing $k_{\mathrm{cut}} = k_{\mathrm{surf}}$. For C1 (C2), $\langle\theta_k\rangle$ has a maximum value of

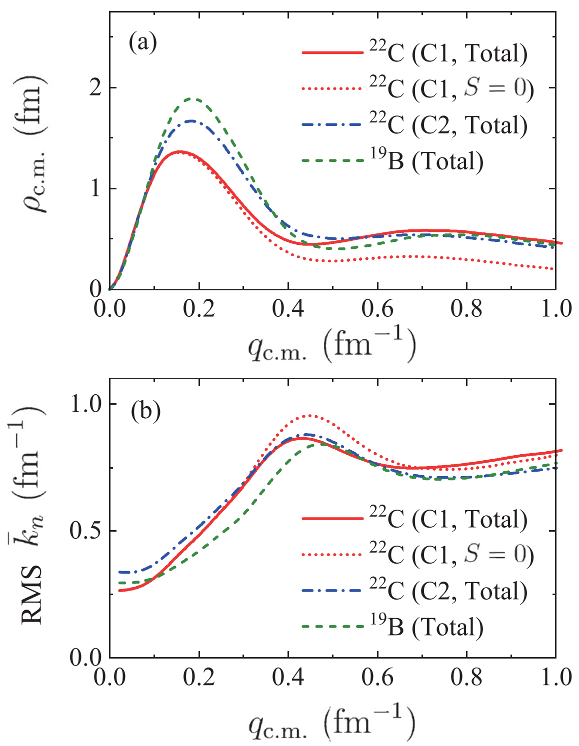

FIG. 9. Same as Fig. 3 but for ^{22}C (sets C1 and C2) and ^{19}B. The result for the $S = 0$ component of ^{22}C (C1) is also shown.

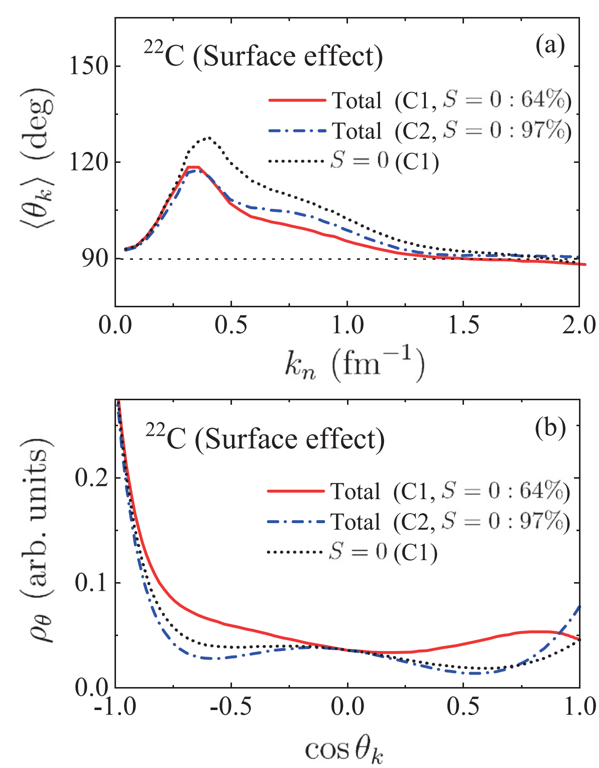

FIG. 10. (a) Mean opening angle $\langle\theta_k\rangle$ for the total $2n$ density of ^{22}C (sets C1 and C2). "Surface effect" indicates the imposed cutoff $k_{\mathrm{cut}} = k_{\mathrm{surf}}$. The result for the $S = 0$ component of ^{22}C (C1) is also shown. (b) The same as (a) but for the opening-angle distribution.

$118^\circ(118^\circ)$ at $k_n = 0.32$ (0.36) fm^{-1}, and it decreases to around 90° at smaller and larger k_n values. Figure 10(a) also shows $\langle\theta_k\rangle$ of the $S = 0$ component for C1. The maximum value of 128° at $k_n = 0.41$ fm^{-1} is large due to the small contribution of the cigarlike and boomerang configurations with smaller θ_k [compare Figs. 8(a) and 8(b)].

Figure 10(b) shows the opening-angle distributions of the total $2n$ density and the $S = 0$ component imposing $k_{\rm cut} = k_{\rm surf}$ for C1. The distribution of the $S = 0$ component has a rather symmetric double-well shape, except for the large dineutron component at $\cos\theta_k < -0.7$. In the distribution for the total $2n$ density, the wells around $\cos\theta_k = 0.72$ and -0.56 are filled by the cigarlike and boomerang configurations, respectively. Figure 10(b) also shows the opening-angle distribution of the total $2n$ density for C2. Similarly to that of the $S = 0$ component for C1, the distribution has a rather symmetric double-well structure.

It is notable that the observation of the angular distribution can give information not only about the dineutron structure but also about the spin-parity of the single-particle resonant states.

VII. APPLICATION TO ^{19}B

For ^{19}B, the observed values of S_{2n} are small but with large uncertainty: 0.089 ± 0.560 MeV [91], 0.14 ± 0.39 MeV [73], and 0.5 ± 0.4 MeV [92]. The recent observation of the $E1$ transition strength suggested $S_{2n} \approx 0.5$ MeV [11].

The analysis of the interaction cross section and the $2n$ separation energy indicates that the valence neutrons are dominantly in the $(d_{5/2})^2$ configuration and the halo formation is suppressed [73,92,93]. The matter radius was extracted as $R_m = 3.11 \pm 0.13$ fm [92].

On the other hand, the upper limit of the s-wave scattering length $a_0 \leqslant -50$ fm was extracted in the decay energy spectrum of ^{18}B studied by a single-proton knockout reaction [94]. The observation of the large $E1$ transition strength of $B(E1) = 1.64 \pm 0.06({\rm stat}) \pm 0.12({\rm sys})\ e^2{\rm fm}^2$ (integrated up to 6 MeV) suggested the large s-wave occupation probability of 35% [11]. The core-$2n$ distance of $5.75 \pm 0.11 \pm 0.21$ fm was extracted based on the three-body model calculation using the ^{17}B-n potential of $a_0 = -50$ fm and the density-dependent contact n-n interaction. Three-body model calculations using the finite-range nn interactions also suggested the large s-wave contribution in ^{19}B [82,95,96].

A. ^{17}B-n potential

I construct the ^{17}B-n potential by modifying the set C1 for ^{22}C, because precise information of ^{18}B is missing at the moment, especially about the d-wave resonant states. The parameters are summarized in Table II.

For the s state, the strength parameter of -36.36 MeV is fixed by $a_0 = -50$ fm. The strength parameter of $V_0 = -37.43$ MeV for the $\ell > 0$ states gives the $d_{5/2}$ resonant state at 1.37 MeV, which is close to the $J^\pi = 1^-$ excited state at 1.14 MeV predicted by a shell model calculation using the WBP interaction [94]. This V_0 is extrapolated by the relation of $V_0 = V_{\rm IS}(1 - \kappa I)$ with $I = (N - Z)/A$ and $\kappa = 0.6185$ [97]. Here, $V_{\rm IS} = -52.94$ MeV is fixed by the experimental value of $S_n = 0.58$ MeV of ^{19}C [72]. This ^{17}B-n potential gives $S_{2n} = 0.490$ MeV, which is close to 0.5 MeV suggested by the recent experiment [11].

B. Three-body structure of ^{19}B

The ground-state properties of ^{19}B are summarized in Table III. The weight of the s state is 54.7%. The core-$2n$ distance of 5.15 fm is smaller than the observed value of $5.75 \pm 0.11 \pm 0.21$ fm [11], while the matter radius of 3.50 fm is larger than the observed value of 3.11(13) fm [92]. Here, the experimental matter radius of 2.99 fm in ^{17}B [92] is used for R_c in Eq. (7).

My result is close to that of the three-body model calculation adopting the similar ^{17}B-n potential plus realistic finite-range nn interactions such as the Gogny-Pires-Tourreil (GPT) potential [96]. The calculation using the GPT potential gives $P[(s_{1/2})^2] = 53.2\%$, $\bar{r}_{c\text{-}2n} = 5.01$ fm, $\bar{r}_{nn} = 7.28$ fm, and $R_m = 3.43$ fm. It was also pointed out that a reduction of the range of the nn interaction causes a significant reduction of $P[(s_{1/2})^2]$. This resembles the smaller value of $P[(s_{1/2})^2] = 35\%$ when the contact nn force was used [11].

While the observed $E1$ strength distribution in ^{19}B is well described within the three-body model assuming the spherical core nucleus [11,96], recent investigations suggested the deformation effect in the ground state of ^{17,19}B [98,99]. So far, it is not clear how to make the large s-wave contribution compatible with the argument of the suppression of the halo formation [73,92,93]. Further analyses are needed to solve the puzzle.

C. Angular correlations in ^{19}B

Figure 7(d) shows the real-space total $2n$ density of ^{19}B. The plot for the $S = 0$ component is almost the same due to $P[S = 0] = 93.9\%$. The overall structure is also similar to that of ^{22}C (C2) with $P[S = 0] = 97.4\%$ [see Fig. 7(c)]. There are three peaks at $(r, \theta_r) = (3.8\ {\rm fm},\ 20^\circ)$, $(3.5\ {\rm fm},\ 156^\circ)$, and $(3.3\ {\rm fm},\ 86^\circ)$ for the dineutron, cigarlike, and boomerang configurations, respectively. The ground-state configuration is mainly the admixture of the same-parity s and d states. The interference with the p states of 2.9% weight causes such a large dineutron component [see also the discussion of the opening-angle distribution in Fig. 11(b)].

Figure 8(d) shows the momentum-space total $2n$ density of ^{19}B. The peak for the dineutron configuration appears at low momentum of $(k_n, \theta_k) = (0.14\ {\rm fm}^{-1},\ 98^\circ)$, while the peaks for the cigarlike and boomerang configurations are at higher momenta of $(k_n, \theta_k) = (0.68\ {\rm fm}^{-1},\ 26^\circ)$ and $(0.59\ {\rm fm}^{-1},\ 98^\circ)$, respectively.

Figure 9(a) shows $\rho_{\rm c.m.}$ obtained from the total $2n$ density of ^{19}B. The peak component below $q_{\rm c.m.} \approx 0.4$ fm^{-1} is large due to the large value of $P[(s_{1/2})^2] = 54.7\%$. The low-$q_{\rm c.m.}$ peak component corresponds the surface region where the $2n$ correlations occur. (It is consistent with the choice of $q_0 = 0.3588$ fm^{-1} for the kSEP interaction as the surface type.)

Figure 9(b) shows $\bar{k}_n$ for ^{19}B. The local maximum value of $\bar{k}_n = 0.86$ fm^{-1} at $q_{\rm c.m.} = 0.47$ fm^{-1} is adopted as the surface

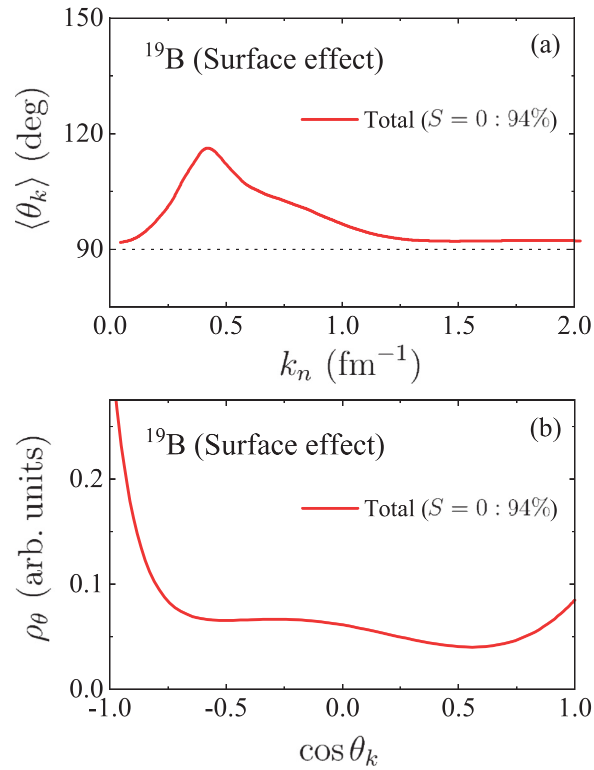

FIG. 11. The same as Fig. 10 but for the total $2n$ density of ^{19}B.

momentum $k_{\rm surf}$. The local maximum value of $\bar{k}_n$ for the $S = 0$ component is the same value, and it determines the long k_n-tail distribution of the $2n$ density [see Fig. 8(d)]. The associated large opening angle, $\theta_{\rm tail} = 2\cos^{-1}[(q_{\rm c.m.}/2)/\bar{k}_n] = 148^\circ$, indicates the strong dineutron correlation.

The mean opening angle and the opening-angle distribution of ^{19}B are also similar to those of ^{22}C (C2). Figure 11(a) shows $\langle\theta_k\rangle$ for the total $2n$ density of ^{19}B imposing $k_{\rm cut} = k_{\rm surf}$. $\langle\theta_k\rangle$ has a maximum value of 117° at $k_n = 0.40$ fm^{-1}, and it approaches to around 90° at smaller and larger k_n values. Figure 11(b) shows the opening-angle distribution of the total $2n$ density for ^{19}B imposing $k_{\rm cut} = k_{\rm surf}$. The opening-angle distribution has rather symmetric double-well structure, except for the large dineutron component at $\cos\theta_k < -0.7$. The opening-angle distribution is similar to the correlation-angle distribution predicted in Ref. [52], except for the divergent behavior around $|\cos\theta_{nf}| \approx 1$.

VIII. SUMMARY

I discussed the momentum-space structure of dineutrons in the Borromean nuclei ^{11}Li, ^{6}He, ^{22}C, and ^{19}B. For this purpose, the three-body model calculation was performed by using a newly constructed finite-range nn interaction in momentum space (the kSEP interaction). The kSEP interaction is easy to handle as the contact $\delta(\mathbf{r})$ interaction. On top of that, it enables us to make a prediction of the spatial structure of dineutrons, which is difficult in calculations using the contact $\delta(\mathbf{r})$ interaction due to the lack of the principal prescription for the cutoff energy.

I showed that the ground-state properties such as the $2n$ separation energy, the matter radius, the core-$2n$ distance, and the n-n distance in ^{11}Li, ^{6}He, and ^{22}C are well reproduced, once the parameters in the kSEP interaction are fixed by the low-energy $^1S_0$ nn scattering and the $2n$ separation energy of ^{11}Li. The weights of the s, p, and d waves are plausible values for the experimental observations and the typical three-body calculations, although the values themselves have a model dependence.

For ^{19}B, the recently extracted value of $S_{2n} \approx 0.5$ MeV [11] is well reproduced, while the matter radius and the core-$2n$ distance are inconsistent with the experimental values. These discrepancies may indicate the deformation effect in ^{17,19}B [98,99], although the observed $E1$ strength distribution was well described within the three-body model assuming a spherical core nucleus [11,96]. Further analyses are needed to solve the puzzle.

The $2n$ densities in momentum space were calculated to see the spatial structure of valence neutrons. In ^{11}Li, the $2n$ density has an asymmetric angular distribution due to the interference of the different-parity s and p states. The peak of the dineutron configuration appears at low core-n momentum k_n with a broad angular distribution. It is accompanied by a long high-k_n tail, which indicates the strong dineutron correlation. The peak for the cigarlike configuration appears at higher k_n.

In ^{22}C and ^{19}B, the ground-state configuration is mainly the admixture of the same-parity s and d states. The $2n$ density has rather symmetric angler distribution, except for the large dineutron component at large opening angle due to the interference with the p states of the small weight. In ^{6}He, the $2n$ density also has rather symmetric angular distribution due to the large 88.4% weight of the p states. The two peaks for the dineutron and cigarlike configurations appear at the same momentum of $k_n \approx 0.4$ fm^{-1}.

I clarified how the mean opening angle and the opening-angle distribution reflect the $2n$ density. In ^{11}Li, ^{22}C, and ^{19}B, the mean opening angle has a maximum value larger than 100° at low k_n, and it decreases to around 90° at lower and higher k_n. The mean opening angle in ^{11}Li well coincides with the observed mean correlation angle, although the reaction mechanism is not considered, except for the cutoff momentum representing the contribution of only halo neutrons. The features of the opening-angle distribution in ^{11}Li are also consistent with those of the observed correlation-angle distribution, if the contribution of only halo neutrons is considered.

For ^{22}C, the influence of the $S = 0$ and 1 components of the $2n$ density was examined by using the ^{20}C-n potentials of C1 ($P[S = 0] = 64\%$) and C2 ($P[S = 0] = 97\%$). A qualitative difference was found in the opening-angle distribution. The distributions for C1 ($S = 0$ component) and C2 (total $2n$ density) have similar symmetric double-well shapes, except for the large dineutron component at $\cos\theta_k < -0.7$. In the distribution for C1 (total $2n$ density), the wells are filled by the cigarlike and boomerang components. For ^{19}B ($P[S = 0] = 94\%$), the mean opening angle and the opening-angle distribution are similar to those of ^{22}C using C2 ($P[S = 0] = 97\%$).

For ^{6}He, the mean opening angle is similar to that in ^{11}Li, but the peak at low k_n is plateaulike due to the broad k_n distribution of the dineutron peak in the $2n$ density. The opening-angle distribution is rather symmetric, except for the large dineutron component at $\cos\theta_k < -0.5$.

In conclusion, I discussed how the mean opening angle and the opening-angle distribution reflect the momentum-space $2n$ density of the Borromean nuclei. I clarified that the study of the angular correlations of halo neutrons is promising for providing rich information about the characteristic dineutron structure in the Borromean nuclei.

ACKNOWLEDGMENTS

I am grateful to T. Nakamura, Y. Kondo, M. Sasano, and M. Honma for valuable comments. Numerical computation in this work was carried out at the Yukawa Institute Computer Facility in Kyoto University.

[1] G. F. Bertsch and H. Esbensen, Ann. Phys. (NY) **209**, 327 (1991).
[2] M. V. Zhukov, B. V. Danilin, D. V. Fedorov, J. M. Bang, I. J. Thompson, and J. S. Vaagen, Phys. Rep. **231**, 151 (1993).
[3] I. Tanihata, J. Phys. G: Nucl. Part. Phys. **22**, 157 (1996).
[4] I. Tanihata, H. Savajols, and R. Kanungo, Prog. Part. Nucl. Phys. **68**, 215 (2013).
[5] M. Matsuo, Phys. Rev. C **73**, 044309 (2006).
[6] K. Hagino, H. Sagawa, J. Carbonell, and P. Schuck, Phys. Rev. Lett. **99**, 022506 (2007).
[7] H. Sagawa and K. Hagino, Eur. Phys. J. A **51**, 102 (2015).
[8] T. Nakamura *et al.*, Phys. Rev. Lett. **96**, 252502 (2006).
[9] T. Aumann *et al.*, Phys. Rev. C **59**, 1252 (1999).
[10] Y. L. Sun *et al.*, Phys. Lett. B **814**, 136072 (2021).
[11] K. J. Cook *et al.*, Phys. Rev. Lett. **124**, 212503 (2020).
[12] G. Ewald *et al.*, Phys. Rev. Lett. **93**, 113002 (2004).
[13] R. Sánchez, W. Nörtershäuser, G. Ewald, D. Albers, J. Behr, P. Bricault, B. A. Bushaw, A. Dax, J. Dilling, M. Dombsky, G. W. F. Drake, S. Götte, R. Kirchner, H.-J. Kluge, T. Kühl, J. Lassen, C. D. P. Levy, M. Pearson, E. Prime, V. Ryjkov, A. Wojtaszek, Z.-C. Yan, and C. Zimmermann, Phys. Rev. Lett. **96**, 033002 (2006).
[14] H. Esbensen, K. Hagino, P. Mueller, and H. Sagawa, Phys. Rev. C **76**, 024302 (2007).
[15] F. M. Marqués *et al.*, Phys. Lett. B **476**, 219 (2000).
[16] F. M. Marqués *et al.*, Phys. Rev. C **64**, 061301(R) (2001).
[17] Y. Kubota *et al.*, Phys. Rev. Lett. **125**, 252501 (2020).
[18] S. Dasgupta, I. Mazumdar, and V. S. Bhasin, Phys. Rev. C **50**, R550(R) (1994).
[19] K. Ueta, H. Miyake, and G. W. Bund, Phys. Rev. C **59**, 1806 (1999).
[20] C. Ji, Ch. Elster, and D. R. Phillips, Phys. Rev. C **90**, 044004 (2014).
[21] H. Kamada, J. Furuya, M. Yamaguchi, and S. Oryu, Few-Body Syst. **57**, 255 (2016).
[22] M. Yamagami, Phys. Rev. C **100**, 054302 (2019).
[23] M. Bender, P.-H. Heenen, and P.-G. Reinhard, Rev. Mod. Phys. **75**, 121 (2003).
[24] J. Dobaczewski, W. Nazarewicz, T. R. Werner, J. F. Berger, C. R. Chinn, and J. Dechargé, Phys. Rev. C **53**, 2809 (1996).
[25] K. Hagino and H. Sagawa, Phys. Rev. C **72**, 044321 (2005).
[26] H. Esbensen, G. F. Bertsch, and K. Hencken, Phys. Rev. C **56**, 3054 (1997).
[27] M. Kortelainen, T. Lesinski, J. Moré, W. Nazarewicz, J. Sarich, N. Schunck, M. V. Stoitsov, and S. Wild, Phys. Rev. C **82**, 024313 (2010).
[28] M. V. Stoitsov, J. Dobaczewski, W. Nazarewicz, S. Pittel, and D. J. Dean, Phys. Rev. C **68**, 054312 (2003).
[29] J. Margueron, H. Sagawa, and K. Hagino, Phys. Rev. C **76**, 064316 (2007).
[30] R. H. Landau, *Quantum Mechanics II: A Second Course in Quantum Theory*, 2nd ed. (John Wiley & Sons, New York, 1996).
[31] J. R. Schrieffer, *Theory Of Superconductivity* (W. A. Benjamin, New York, 1964).
[32] T. Alm, B. L. Friman, G. Röpke, and H. Schulz, Nucl. Phys. A **551**, 45 (1993).
[33] A. Osman, Phys. Rev. C **19**, 1127 (1979).
[34] A. Schnell, G. Röpke, and P. Schuck, Phys. Rev. Lett. **83**, 1926 (1999).
[35] A. D. Sedrakian, D. Blaschke, G. Röpke, and H. Schulz, Phys. Lett. B **338**, 111 (1994).
[36] M. Beyer, G. Röpke, and A. Sedrakian, Phys. Lett. B **376**, 7 (1996).
[37] W. Schadow, W. Sandhas, J. Haidenbauer, and A. Nogga, Few-Body Syst. **28**, 241 (2000).
[38] P. Bożek and P. Czerski, Eur. Phys. J. A **11**, 271 (2001).
[39] Y. Dewulf, W. H. Dickhoff, D. Van Neck, E. R. Stoddard, and M. Waroquier, Phys. Rev. Lett. **90**, 152501 (2003).
[40] H. Stein, A. Schnell, T. Alm, and G. Röpke, Z. Phys. A **351**, 295 (1995).
[41] M. Jin, M. Urban, and P. Schuck, Phys. Rev. C **82**, 024911 (2010).
[42] N. Martin and M. Urban, Phys. Rev. C **90**, 065805 (2014).
[43] Y. Tian, Z. Y. Ma, and P. Ring, Phys. Lett. B **676**, 44 (2009).
[44] H. Tajima, T. Hatsuda, P. van Wyk, and Y. Ohashi, Sci. Rep. **9**, 18477 (2019).
[45] Y. Yamaguchi, Phys. Rev. **95**, 1628 (1954).
[46] Y. Kikuchi, K. Katō, T. Myo, M. Takashina, and K. Ikeda, Phys. Rev. C **81**, 044308 (2010).
[47] Y. Kikuchi, K. Ogata, Y. Kubota, M. Sasano, and T. Uesaka, Prog. Theor. Exp. Phys. **2016**, 103D03 (2016).
[48] I. J. Thompson, F. M. Nunes, and B. V. Danilin, Comput. Phys. Commun. **161**, 87 (2004).
[49] M. Rodríguez-Gallardo, J. M. Arias, J. Gómez-Camacho, A. M. Moro, I. J. Thompson, and J. A. Tostevin, Phys. Rev. C **72**, 024007 (2005).
[50] M. Smith *et al.*, Phys. Rev. Lett. **101**, 202501 (2008).
[51] B. M. Young *et al.*, Phys. Rev. C **49**, 279 (1994).
[52] J. Casal and M. Gómez-Ramos, Phys. Rev. C **104**, 024618 (2021).
[53] Y. Kikuchi, T. Myo, K. Katō, and K. Ikeda, Phys. Rev. C **87**, 034606 (2013).
[54] T. Myo, Y. Kikuchi, K. Katō, H. Toki, and K. Ikeda, Prog. Theor. Phys. **119**, 561 (2008).

[55] M. Gómez-Ramos, J. Casal, and A. M. Moro, Phys. Lett. B **772**, 115 (2017).
[56] M. Matsuo, K. Mizuyama, and Y. Serizawa, Phys. Rev. C **71**, 064326 (2005).
[57] C. A. Bertulani and M. S. Hussein, Phys. Rev. C **76**, 051602(R) (2007).
[58] A. Ozawa, T. Suzuki, and I. Tanihata, Nucl. Phys. A **693**, 32 (2001).
[59] A. V. Dobrovolsky *et al.*, Nucl. Phys. A **766**, 1 (2006).
[60] M. Brodeur *et al.*, Phys. Rev. Lett. **108**, 052504 (2012).
[61] D. R. Tilley *et al.*, Nucl. Phys. A **708**, 3 (2002).
[62] Y. Aksyutina *et al.*, Phys. Lett. B **679**, 191 (2009).
[63] B. V. Danilin, I. J. Thompson, J. S. Vaagen, and M. V. Zhukov, Nucl. Phys. A **632**, 383 (1998).
[64] L. V. Chulkov and G. Schrieder, Z. Phys. A **359**, 231 (1997).
[65] Z.-T. Lu, P. Mueller, G. W. F. Drake, W. Nörtershäuser, and Steven C. Pieper, and Z.-C. Yan, Rev. Mod. Phys. **85**, 1383 (2013).
[66] I. Tanihata *et al.*, Phys. Lett. B **289**, 261 (1992).
[67] J. S. Al-Khalili, J. A. Tostevin, and I. J. Thompson, Phys. Rev. C **54**, 1843 (1996).
[68] J. A. Tostevin and J. S. Al-Khalili, Nucl. Phys. A **616**, 418 (1997).
[69] H. Simon *et al.*, Phys. Rev. Lett. **83**, 496 (1999).
[70] H. Simon *et al.*, Nucl. Phys. A **791**, 267 (2007).
[71] L. V. Chulkov *et al.*, Phys. Rev. Lett. **79**, 201 (1997).
[72] G. Audi, A. H. Wapstra, and C. Thibault, Nucl. Phys. A **729**, 337 (2003).
[73] L. Gaudefroy *et al.*, Phys. Rev. Lett. **109**, 202503 (2012).
[74] K. Tanaka *et al.*, Phys. Rev. Lett. **104**, 062701 (2010).
[75] Y. Togano *et al.*, Phys. Lett. B **761**, 412 (2016).
[76] N. Kobayashi *et al.*, Phys. Rev. C **86**, 054604 (2012).
[77] S. Mosby *et al.*, Nucl. Phys. A **909**, 69 (2013).
[78] M. Yamashita, R. M. de Carvalho, T. Frederico, and L. Tomio, Phys. Lett. B **697**, 90 (2011).
[79] M. Yamashita, R. M. de Carvalho, T. Frederico, and L. Tomio, Phys. Lett. B **715**, 282 (2012).
[80] Y. Kucuk and J. A. Tostevin, Phys. Rev. C **89**, 034607 (2014).
[81] S. N. Ershov, J. S. Vaagen, and M. V. Zhukov, Phys. Rev. C **86**, 034331 (2012).
[82] T. Suzuki and T. Otsuka, Few-Body Syst. **62**, 32 (2021).
[83] T. Suzuki, T. Otsuka, C. Yuan, and A. Navin, Phys. Lett. B **753**, 199 (2016).
[84] B. Acharya, C. Ji, and D. R. Phillips, Phys. Lett. B **723**, 196 (2013).
[85] W. Horiuchi and Y. Suzuki, Phys. Rev. C **74**, 034311 (2006).
[86] V. Maddalena *et al.*, Phys. Rev. C **63**, 024613 (2001).
[87] I. Hamamoto, Phys. Rev. C **93**, 054328 (2016).
[88] E. C. Pinilla and P. Descouvemont, Phys. Rev. C **94**, 024620 (2016).
[89] J. Singh, W. Horiuchi, L. Fortunato, and A. Vitturi, Few-Body Syst. **60**, 50 (2019).
[90] N. A. Orr, EPJ Web Conf. **113**, 06011 (2016).
[91] M. Wang *et al.*, Chin. Phys. C **41**, 030003 (2017).
[92] T. Suzuki *et al.*, Nucl. Phys. A **658**, 313 (1999).
[93] H. T. Fortune and R. Sherr, Eur. Phys. J. A **48**, 103 (2012).
[94] A. Spyrou *et al.*, Phys. Lett. B **683**, 129 (2010).
[95] E. Hiyama, R. Lazauskas, F. M. Marqués, and J. Carbonell, Phys. Rev. C **100**, 011603(R) (2019).
[96] J. Casal and E. Garrido, Phys. Rev. C **102**, 051304(R) (2020).
[97] A. Bohr and B. R. Motteleson, *Nuclear Structure*, Vol. I (W. A. Benjamin, New York, 1969).
[98] X.-X. Sun, Phys. Rev. C **103**, 054315 (2021).
[99] Z. H. Yang *et al.*, Phys. Rev. Lett. **126**, 082501 (2021).